

Research on Multiphysics Coupling Fields in Electrochemical Trepanning of Lateral Flow

Gaopan Lei

Nanjing University of Aeronautics and Astronautics

Dong Zhu (✉ zhudong@nuaa.edu.cn)

Nanjing University of Aeronautics and Astronautics

Di Zhu

Nanjing University of Aeronautics and Astronautics

Research Article

Keywords: multiphysics coupling, simulation, electrochemical trepanning, machining accuracy, surface quality

Posted Date: June 1st, 2021

DOI: <https://doi.org/10.21203/rs.3.rs-188564/v1>

License:  This work is licensed under a Creative Commons Attribution 4.0 International License.

[Read Full License](#)

Version of Record: A version of this preprint was published at The International Journal of Advanced Manufacturing Technology on January 14th, 2022. See the published version at

<https://doi.org/10.1007/s00170-022-08651-0>.

Research on multiphysics coupling fields in electrochemical trepanning of lateral flow

Gaopan Lei, Dong Zhu*, Di Zhu

College of Mechanical & Electrical Engineering, Nanjing University of Aeronautics and Astronautics, Nanjing, 210016, China

*Corresponding author at: Nanjing University of Aeronautics and Astronautics, 29 Yudao Street, Nanjing, 210016, China.

E-mail address: zhudong@nuaa.edu.cn

Abstract

Electrochemical trepanning (ECTr) is an effective method for machining the ruled surface parts. Generally, the forward flow mode is used in ECTr. Under the forward flow, the streamlines at the outlet are divergent, resulting in the obvious flow patterns at the outlet and the instability of the machining process. In ECTr of a diffuser with a special structure, the lateral flow mode is adopted to improve the uniformity of the flow field, thereby improving the surface quality at the hub. ECTr is a complicated multiphysics coupling process. To investigate the distributions of electric field, two-phase flow field and thermal field in ECTr with lateral flow, a multiphysics coupling field model was established. In this model, a coupling relationship was formed between the various physical fields through the change of the electrolyte conductivity. Through the multiphysics coupling simulation, the changes of the gas bubbles volume fraction, the electrolyte temperature, the electrolyte conductivity and the current density were obtained along the flow path. Compared with the inlet of the electrolyte, the gas bubbles volume fraction and the temperature at the outlet increased by 38.8% and 6.3 K, respectively. Under the combined influence, the conductivity decreased by 7.227 S/m at the outlet, resulting in a decrease of 57.81 A/cm² in the current density. Then, the corresponding experiment of lateral flow ECTr was performed to verify the simulation results. Along the flow path, the thickness of the machined blade gradually increased, varying from 2.09 mm to 2.76 mm. The surface quality gradually deteriorated along the flow path and the surface roughness varied from Ra 0.72 μm to Ra 1.05 μm. Combining the simulation and the experiment, the correctness and the effectiveness of the multiphysics coupling model and simulation were confirmed. The results can be applied to other ECM processes.

Keywords: multiphysics coupling, simulation, electrochemical trepanning, machining accuracy, surface quality

1. Introduction

Electrochemical machining (ECM) is based on electrochemical anodic dissolution, which is a multiphysics coupling process [1]. The process involves flow field, electric field, thermal field etc. Each physical field influences each other and the relationships between various physical fields are very complicated [2]. To improve the machining quality of ECM in a targeted manner, it is very important to observe the distribution of various physical fields.

Numerous researchers have conducted a large number of simulation studies to analyze the distribution of physical field in ECM. By analyzing the flow field, the cathode structure was optimized during ECM of the internal spiral tube [3]. The uniformity of the flow field was improved through a special structure of the cathode [4]. Through establishing electric field model, Skinn et al compared primary current distribution simulations with indentations fabricated by ECM of steel panels [5]. The distribution of the current density under a flexible auxiliary electrode mechanism was obtained in counter-rotating ECM [6]. By establishing the thermal field model in ECM, Clark and Mcgeough analyzed the distribution of temperature along the machining gap [7]. To observe the temperature distribution in aqueous NaNO₃ electrolyte solution, the simulations of thermal field was performed [8, 9]. Although the distributions of the analyzed field state can be reflected to a certain extent under the single corresponding physical field simulation, the status of other physical fields in the machining area cannot be obtained. Because of the characteristics of the multi-physical coupling process for ECM, it is essential to develop the analysis of multiphysics coupling field for further enhancing the machining quality.

To present a more realistic state in ECM, some studies of multiphysics coupling fields have been explored. Mi et al established the model of electric field and two-phase flow field coupling without considering the change of the electrolyte temperature [10]. Through the finite element method, Gomez-Gallegos et al. carried out the multiphysics coupling simulation, which combined the electric field, flow field and thermal field with ignoring the generated bubbles [11]. To observe the distributions of whole physical fields accurately, Klocke et al. set up an interdisciplinary simulation model for aero engine blade and the model involved two-phase flow field, electric field and thermal field [12]. Under the same physical fields coupling conditions, Chang and Hourng established a two-dimensional numerical model to guide cathode design [13]. Schaarschmidt et al achieved the simulation to examine the differences between front and lateral working gap in the pulsed ECM process with oscillating cathode [14]. Under the multi-physics coupling analysis, a state closer to the actual processing was visually presented. In view of the uneven distributions of the physical fields that may occur in the processing, the problems can be predicted and be

better avoided in advance.

As an effective style of ECM, electrochemical trepanning (ECTr) has unique advantages in machining the ruled surface parts, which processes the parts through the relative movement between the hollow shaped cathode sheet and the workpiece. In ECTr, the forward flow mode is used generally. By analyzing the flow field, Zhu et al developed a dynamic lateral flow method to improve the uniformity of flow field for enhancing the surface quality at the electrolyte outlet [15]. Through the analysis of the electric field, the method of cathode tool design was developed under iterative correction [16]. However, the main simulation analysis in ECTr is a single physical field currently, there are few literatures publicly on the multiphysics coupling simulation. This paper focuses on the distributions of physical fields in ECTr of lateral flow under the analysis of multiphysics coupling.

For investigating the distribution of each physical field in ECTr, a model was established, which involved electric field, two-phase flow field and thermal field. Through the multiphysics coupling simulation, the changes of the gas bubbles volume fraction, the electrolyte temperature, the electrolyte conductivity and the current density in machining gap were examined along the flow path. Then, a series of corresponding experiment of ECTr was performed to verify the simulation results. Through analyzing the machining accuracy and the surface quality of the machined blade, the simulation results were verified effectively.

2. Description of electrochemical trepanning

In ECM, the machining quality is determined by the effect of multi-physics coupling. The physical fields interact with each other and the connections of each physical field are shown in Fig.1 [17, 18, 19]. As a voltage is applied on the electrodes, the electrochemical reaction is occurred and the material is quickly removed. During the process, in electric field, the hydrogen bubbles are continuously generated on the cathode surface with the transfer of electrons in electrolyte under the hydrogen evolution reaction and the Joule heat is produced because of the current heating effect. The electrolyte velocity in the flow field is affected by the generated bubbles and the temperature in the thermal field is influenced by the Joule heat. The conductivity of the electrolyte is related to the gas bubbles volume fraction and the temperature. The current density in the electric field is impacted by the conductivity and the machining gap. Therefore, the flow field and the thermal field will interact with the electric field. The flow field and the thermal field influence each other through the thermal conduction and the dynamic viscosity. Because the material removal rate in ECM is associated with the current density and the electric field distribution is closely related to other physical fields, the forming accuracy and surface quality are the result of multiple fields simultaneously.

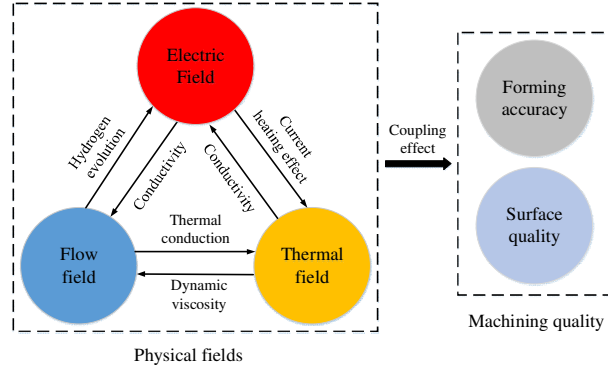


Fig.1. Relationship between physical fields and machining quality in ECM.

ECTr is an effective method of ECM. During the ECTr process, the shaped cathode of a hollow sheet is fed to the workpiece at a preset speed with the electrolyte flowing and a blade is formed. To protect the machined blade, an insulator is placed in the inner cavity of the cathode. In ECM, according to the flow path and the flow direction of electrolyte in machining gap, there are three main flow modes: forward flow, reverse flow and lateral flow. Generally, the forward flow mode is adopted in ECTr. Under forward flow mode, the electrolyte streamlines are divergent at the outlet because the flow channels becomes large greatly. Owing to the uneven flow field distribution, an unstable machining process may occur. And, a poor surface quality may be presented at the outlet, for example obvious flow patterns. To improve the distribution of the flow field and obtain a better surface quality at the outlet, the other modes is tried in ECTr. Compared with the forward flow, the lateral flow can obtain a stable flow state, and it is easier to achieve in actual processing than the reverse flow [20]. So, the lateral flow mode is adopted.

In ECTr with lateral flow, the electrolyte flows from the leading edge to the trailing edge in electrode gap, as shown in Fig.2. With electrolyte flowing, the produced gas bubbles and heat are moved from inlet to outlet during machining, causing a difference on the conductivity along the flow path. That may result in certain changes for the current density and the material removal rate in different regions. So, because of the uneven physical field distribution, the inconsistent machining quality along the flow path may be occurred. To investigate the distributions of various physical fields in ECTr, the multiphysics coupling simulation will be carried out in following parts.

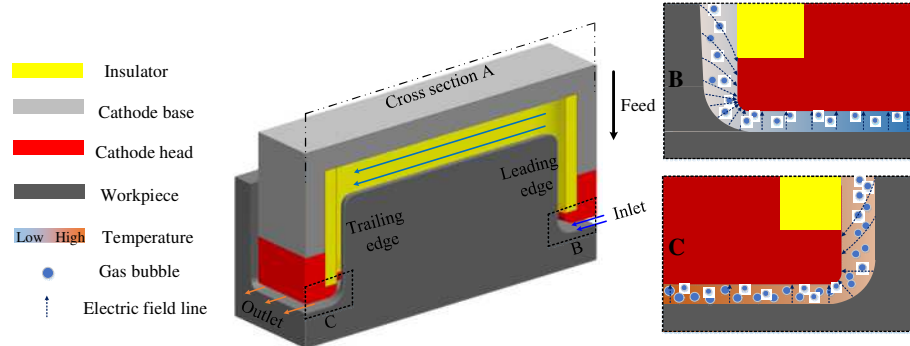


Fig.2. Schematic diagram for ECTr of lateral flow.

3. Simulation

To examine the distribution of each physical field, a mathematical model of material dissolution of ECTr was established. Then, the multiphysics coupling simulation of ECTr was performed to observe the changes in physical quantities along the flow path, such as the gas bubbles volume fraction, the temperature, the conductivity and the current density.

3.1 Mathematical model

During the ECTr, the processing voltage is loaded on the electrodes. The distribution of electric field between electrodes satisfies the Laplace's equation, which is described as follows [21]:

$$\nabla^2 \phi = 0 \quad (1)$$

where ϕ is the electrical potential in the inter-electrode gap.

In electric field, the relationship between the current density and the electric field strength and the conductivity is as follows :

$$i = \kappa E \quad (2)$$

where i is the current density, κ is the electrical conductivity of the electrolyte and E is the electric field strength.

The conductivity of the electrolyte is related to the gas bubbles volume fraction and the electrolyte temperature, which can be considered as following equation [26]:

$$\kappa = \kappa_0 (1 - \beta^g)^{bp} (1 + \alpha(T - T_0)) \quad (3)$$

where κ_0 is the initial conductivity of the electrolyte, β^g is the gas volume fraction of the electrolyte, bp is the Bruggeman's coefficient, α is the temperature coefficient of the conductivity, T is the electrolyte temperature and T_0 is the original temperature of the electrolyte. The bp is generally 1.5~2 and it will be taken 1.5 here and α will be taken 0.2911 1/K.

As the machining proceeding, some hydrogen bubbles are generated on the cathode surface with the transfer of electrons. According to the Faraday's laws, the flux of the produced gases can be described by the following equation [23]:

$$N_{H_2} = \frac{i}{2F} = \frac{\kappa E}{2F} \quad (4)$$

where F is the Faraday's constant.

In flow field of ECTr, because the electrolyte flow is a gas-liquid mixing flow, the density and dynamic viscosity of the flow satisfy the following relationships [24]:

$$\begin{aligned} \rho &= \beta^g \rho_1 + \beta^l \rho_2 \\ \mu &= \beta^g \mu_1 + \beta^l \mu_2 \end{aligned} \quad (5)$$

where ρ is the electrolyte density, β is the volume fraction, ρ_1 is the gas density, ρ_2 is the liquid density, g is the gas and μ is the dynamic viscosity.

The flow model is a complex curved flow and the Re-normalization group (RNG) $k-\epsilon$ model is suitable for solving this complicated flow field state, so RNG $k-\epsilon$ model is adopted here. The flow state of incompressible fluid can be governed by the following Navier-Stokes equation and continuity equation [25]:

$$\begin{aligned} -\mu \nabla^2 u + \rho(u \cdot \nabla)u + \nabla p &= 0 \\ \nabla \cdot u &= 0 \end{aligned} \quad (6)$$

where u is the flow rate and p is the electrolyte pressure.

In thermal field of ECTr, owing to the current heating effect, the Joule heat is produced during the process. And it is considered that the Joule heat is not dissipate here. The temperature distribution is calculated by solving convection-diffusion equations with heat sources [26] as follows:

$$\begin{aligned} \rho C_p \frac{\partial T}{\partial t} + \rho C_p u \cdot \nabla T + \nabla \cdot q &= Q \\ q &= -\lambda \nabla T \\ Q &= i \cdot E = \kappa E^2 \end{aligned} \quad (7)$$

Where C_p is the specific heat capacity coefficient of the electrolyte, q is the heat flux, λ is the thermal conductivity and Q is the heat source (ohmic heating).

3.2 Simulation model

To simplify the model, a geometric model of the simulation was established based on cross section A (Fig.3), the position of which is in the middle profile from inlet to outlet (Fig2).

In the geometric model, the inter-electrode gap (Δ) between the cathode head and the workpiece was equal to 0.4 mm, the height of the cathode slice (a) was adopted to 1 mm, the width of the cathode base (b) was equal to 1.6 mm, the width of the insulator (c) was also equal to 1.6 mm, the height of the insulator (d) was equal to 10 mm, the width of the cathode cavity (e) was equal to 23.6 mm, the length of workpiece (f) was equal to 30 mm, and the fillet radii at the cathode edge fillet (r_1) was 0.8 mm.

For simplifying the simulation, several assumptions were adopted. (1) The oxygen generated on the workpiece was ignored. (2) The generated Joule heat did not escape. (3) There was no slip at the boundary. Above the conditions, the boundary conditions on the geometric model were set follow:

$$\frac{\partial \varphi}{\partial n} \Big|_{\Gamma_{1,8}} \approx 0 \quad (\text{Free boundaries}) \quad (8)$$

$$\varphi \Big|_{\Gamma_{2,7}} = 0 \quad (\text{On the cathode}) \quad (9)$$

$$\frac{\partial \varphi}{\partial n} \Big|_{\Gamma_{3,4,6}} = 0 \quad (\text{Insulation boundaries}) \quad (10)$$

$$\varphi \Big|_{\Gamma_5} = U \quad (\text{On the workpiece}) \quad (11)$$

$$p \Big|_{\Gamma_1} = p_1 \quad (\text{Electrolyte inlet}) \quad (12)$$

$$p \Big|_{\Gamma_8} = p_2 \quad (\text{Electrolyte outlet}) \quad (13)$$

Where n was the unit normal vector surface.

According to Eq.3, the conductivity of the electrolyte was set in the solution domain. When the conductivity changed, it causes the current density in the electric field to change, which led to the change of the amount of generated gas and generated Joule heat. Along with the electrolyte flowing, the gas bubble volume fraction and temperature of the electrolyte in the processing zone occurred a certain difference. At the same time, the conductivity was determined by the gas bubble volume fraction and temperature. So, the coupling relationship was formed between each physical field through the change of the conductivity.

Then, the condition parameters of the multiphysics coupling simulation were set according to the actual processing conditions (Table 1) and the corresponding simulation was performed.

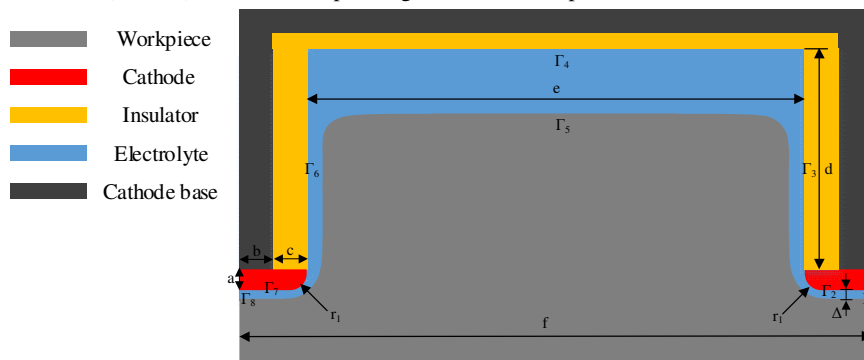


Fig.3.Simulation geometric model of ECTr with lateral flow.

Table 1.Simulation condition parameters

Condition	Value
Processing voltage (U)	25 V
Electrolyte	20% w.t NaNO ₃
Inlet pressure (p_1)	1.0 MPa
Outlet pressure(p_2)	0 MPa
Electrolyte initial conductivity (κ)	14.6 S/m
Electrolyte initial temperature (T_0)	303.15 K

3.3 Simulation results

Through the multiphysics coupling simulation, the distributions of physical fields were obtained. In addition, the change curves of each parameter value were presented along the flow path at the middle of the machining gap. Based on the changes of various physical parameters, the possible effects on the machining accuracy and surface quality of machined blade were analyzed in detail.

3.3.1 Gas bubbles volume fraction

To analyze the change from the inlet to the outlet, a detection line (*B*) was taken, which was located at a distance of 0.2 mm from the workpiece surface because of the inter-electrode gap of 0.4 mm (Fig.4). In ECTr, according to Eq.4, the hydrogen gas bubbles were continuously generated on the surface of the cathode with the material removal. As the electrolyte flowing, the gas bubbles were stacked along the flow path. The distribution cloud and the change curve on line *B* of the gas bubbles volume fraction were achieved, as shown in Fig.5.

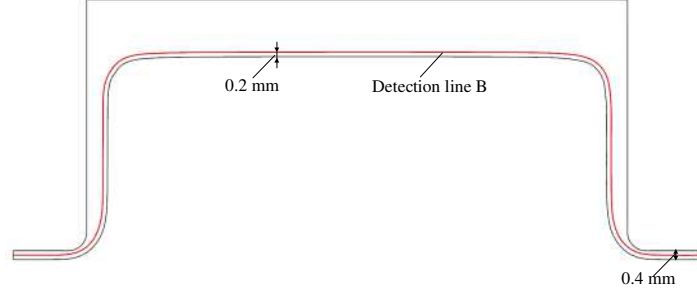


Fig.4 Detection line in the simulation.

From the Fig.5 (a), the gas bubbles volume fraction gradually increased and changed significantly along the flow path from the inlet to the outlet. From the Fig.5 (b), the values at the inlet and the outlet were respectively 0 and 38.8%. It was considered that the electrolyte at the inlet was pure without gas bubbles. With the electrolyte flowing, the gas bubble volume fraction reached 38.8% because of the gas bubbles gathering at the outlet.

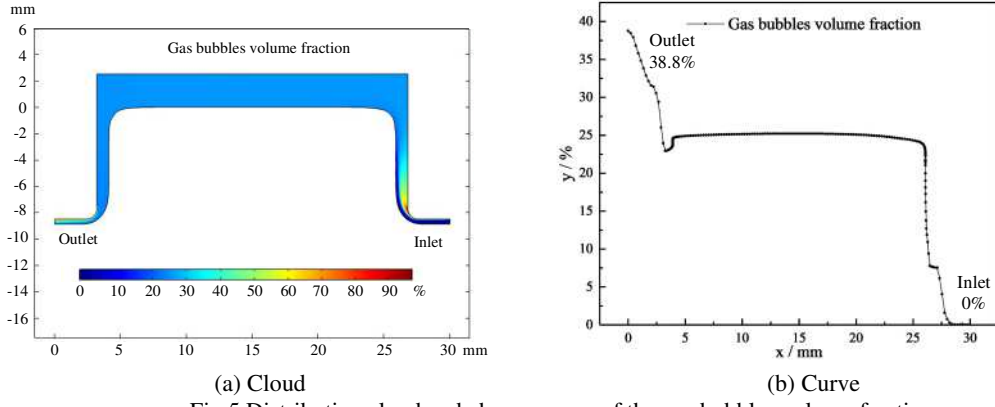
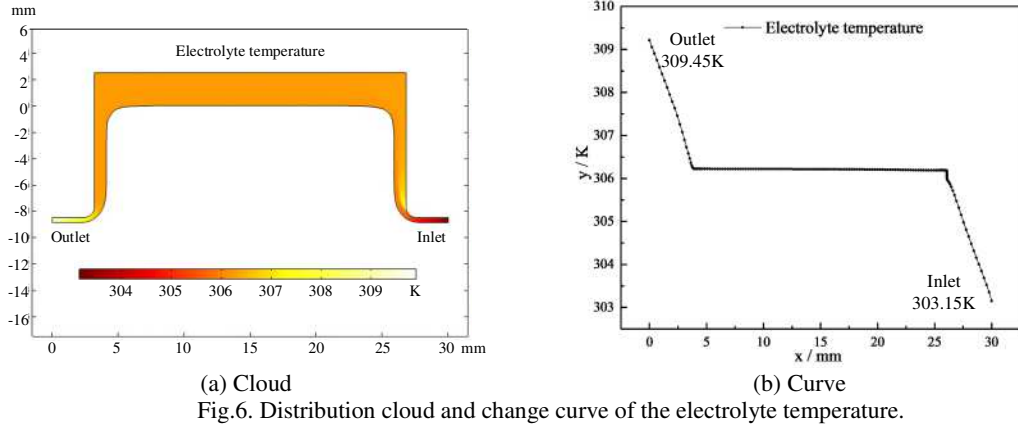


Fig.5 Distribution cloud and change curve of the gas bubbles volume fraction.

3.3.2 Electrolyte temperature

Based on Eq.7, the Joule heat was generated and the electrolyte temperature was related to the electrolyte flow rate and the gas bubbles volume fraction. The distribution cloud and the change curve of the electrolyte temperature were obtained, as shown in Fig.6.

With the electrolyte flowing, the generated heat was moved along the flow path. In Fig.6 (a), the electrolyte temperature changed smoothly and gradually increased along the flow path. From Fig.6 (b), the values at the inlet and the outlet were 303.15 K and 309.45 K, respectively. And the temperature of the electrolyte at the outlet was 6.3 K higher than that at the inlet.

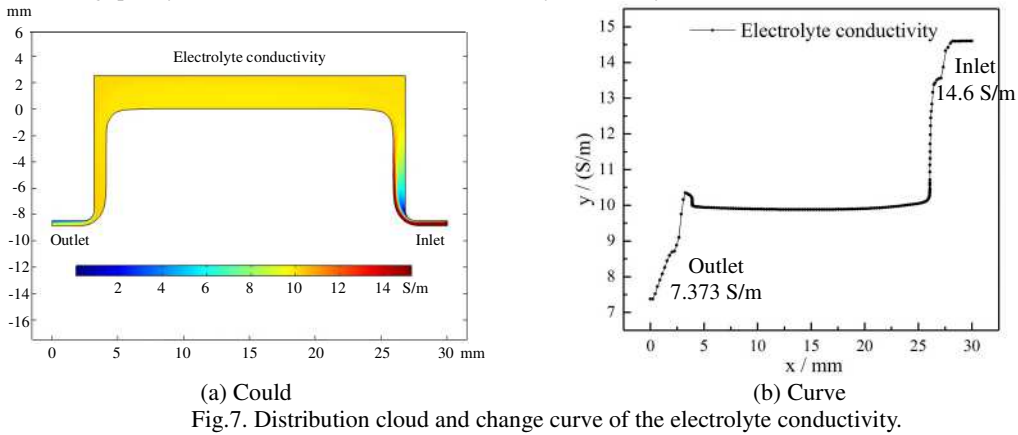


3.3.3 Electrolyte conductivity

The conductivity of the electrolyte was associated with the gas bubbles volume fraction, the temperature and the electrolyte characteristic in Eq.3. Under a single variable, when the gas bubbles volume fraction increase or the temperature dropped, the conductivity decreased. The electrolyte conductivity distributions at different regions were achieved (Fig.7 (a)) and the change curve of the conductivity was obtained along the flow path (Fig.7 (b)).

From above results, under the influence of comprehensive factors, the electrolyte conductivity had a certain corresponding change from the inlet to the outlet. From the Fig.7 (a), the conductivity at the inlet was significantly greater than that at the outlet. According to the Fig.7 (b), the conductivity of the electrolyte at the inlet and the outlet were 14.600 S/m and 7.373 S/m, respectively. The difference between them could reach 7.227 S/m.

At the inlet, the gas bubbles volume fraction of the electrolyte was 0% and the temperature of the electrolyte did not change, which was the initial value, so the value of the conductivity remained consistent with the initial solution property value. As the electrochemical machining process, the gas bubbles and Joule heat were produced. The gas bubbles volume fraction and temperature gradually increased along the flow path. And the gas bubbles volume fraction dominated the entire process and played a leading role. That had a greater impact on the conductivity. Thus, the change trend of the conductivity was opposite to the change trend of the gas bubbles volume fraction. Even if the temperature of the electrolyte at the outlet was 6.3 K higher than that at the inlet, the conductivity value dropped sharply. Since the distributions of the conductivity directly affected the current density of each area, thereby affecting the machining quality, the distributions of the current density were analyzed below.

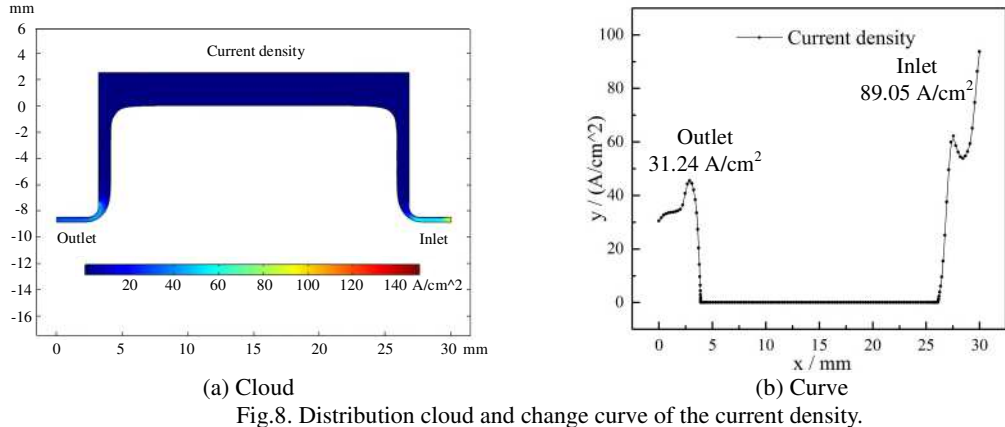


3.3.4 Current density

The current density directly affected the material removal rate to influence the machining quality of the machined blade. To examine the machining quality of each area, the distribution cloud and the change curve on the detection line of the current density were achieved, as shown in Fig.8.

The conductivity of the electrolyte was an important influence factor of the current density. From above results, the electrolyte conductivity had a difference in various regions. The region where the current was maximum was same as the value where the conductivity was the largest. From the Fig.8 (a), the value at the inlet region was obviously greater than that at the outlet region. According to the Fig.8 (b), the current density value was 89.05 A/cm² at the inlet. However it was only 31.24 A/cm² at outlet. The difference between the two regions reached 57.81 A/cm². The material removal rate is proportional to the current density. Thus, more material will be removed at the inlet than at the outlet. As a result, the thickness of the machined blade may increase accordingly along the flow path.

Generally, when the current density is higher, the surface processed becomes smoother. Thus, according to the above results, the surface quality of the machined blade may gradually deteriorate along the flow path because of the decrease of the current density.



4. Experiment and analysis

To verify the simulation results, the ECTr experiment will be carried out. And through measuring the thickness and surface roughness of each area for the machined blade, the machining accuracy and the surface quality can be evaluated.

4.1 Establishment of experiment

In the experiment, the combined cathode used (Fig.9 (a)) was made up of the cathode sheet, the cathode base and the insulator. The entire geometric shape was consistent with the model used in the above simulation. Through designing a new special fixture, the lateral flow mode of the electrolyte was achieved. The combined fixture adopted and the processing schematic sketch were presented (Fig.9 (b)). The workpiece material was Inconel 625. The feeding rate and the feeding distance of the cathode were adopted as 1.6 mm/min and 9 mm. The other machining parameters used in this experiment were the same as those in the simulation (Table 1).

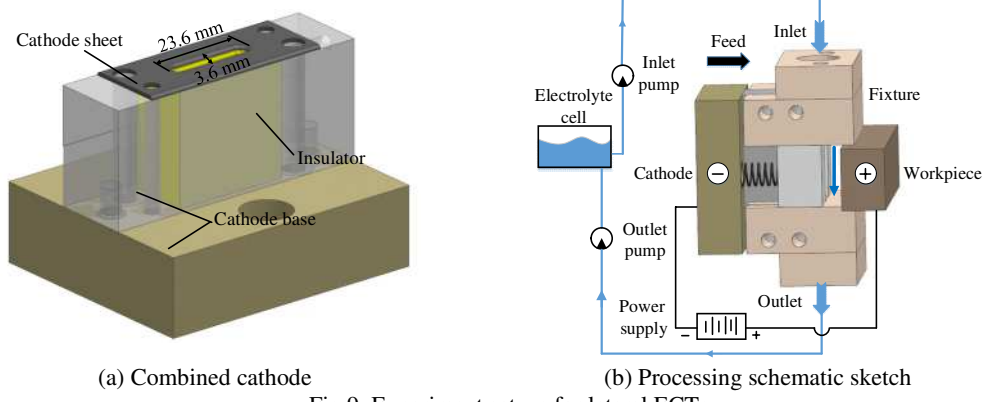
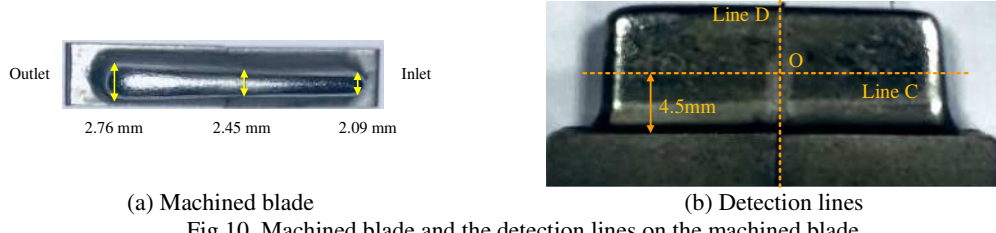


Fig.9. Experiment set-up for lateral ECTr.

4.2 Experiment results and analysis

Through the experiment of the ECTr, the machined blade was obtained (Fig.10 (a)). To analyze the machining accuracy and the surface quality on different regions, two detection lines were taken on the blade (Fig.10 (b)). Line C was a horizontal line located 4.5 mm from the bottom along the flow path and line D was vertical line in the middle of the blade length. The intersection between the two lines was O point. The machining accuracy and the surface quality were judged by the thickness and the surface roughness of the blade machined, respectively.



(a) Machined blade (b) Detection lines

Fig.10. Machined blade and the detection lines on the machined blade.

4.2.1 Machining accuracy

Through measuring the thickness of the machined blade, there were obvious varieties along the flow way. The thickness changed from 2.09 mm to 2.45 mm and then to 2.76 mm from the inlet to the outlet on the line C. The thickness difference was 0.67 mm. And along the line D, the thickness of the machined blade gradually became thinner from bottom to top, ranging from 2.56 mm to 2.04 mm.

According to the simulation results above, the gas bubbles volume fraction, the temperature, the conductivity and the current density changed along the flow path. Because the conductivity of the electrolyte gradually decreased along the flow path, the current density had the same trend. That caused the current density was different along the flow path. From the inlet to the outlet, the current density value decreased from 89.05 A/cm^2 to 31.24 A/cm^2 and the material removal rate also gradually reduced according to the Faraday's Law. In the same plane, the larger material removal rate may lead to the smaller thickness of the machined blade. So, the thickness of the machined blade will increase accordingly along the flow path. In the experiment, the variety of the thickness of the machined blade from the inlet to the outlet was consistent with the simulation prediction results.

From the distribution of current density obtained above, the blade tip region still had weak current. Under the stray current effecting, the machined blade suffered secondary corrosion. The stray corrosion caused that the thickness of the machined blade gradually decreased from the root to the tip on the line D, resulting in a certain taper degree.

4.2.2 Surface quality

The surface roughness of the machined blade was obtained via using Form Talysurf i-Series 5 surface measurement. The three-dimensional surface topography and surface roughness curve along the flow path were achieved (Fig.11). The surface roughness changed from $R_a 0.72 \mu\text{m}$ to $R_a 0.79 \mu\text{m}$ and then to $R_a 1.05 \mu\text{m}$ from inlet to outlet along the line C. The difference of the surface roughness was $R_a 0.33 \mu\text{m}$. From the blade tip to the blade root, the surface roughness values gradually increased, varying from $R_a 0.62 \mu\text{m}$ to $R_a 0.79 \mu\text{m}$ and then to $R_a 0.97 \mu\text{m}$.

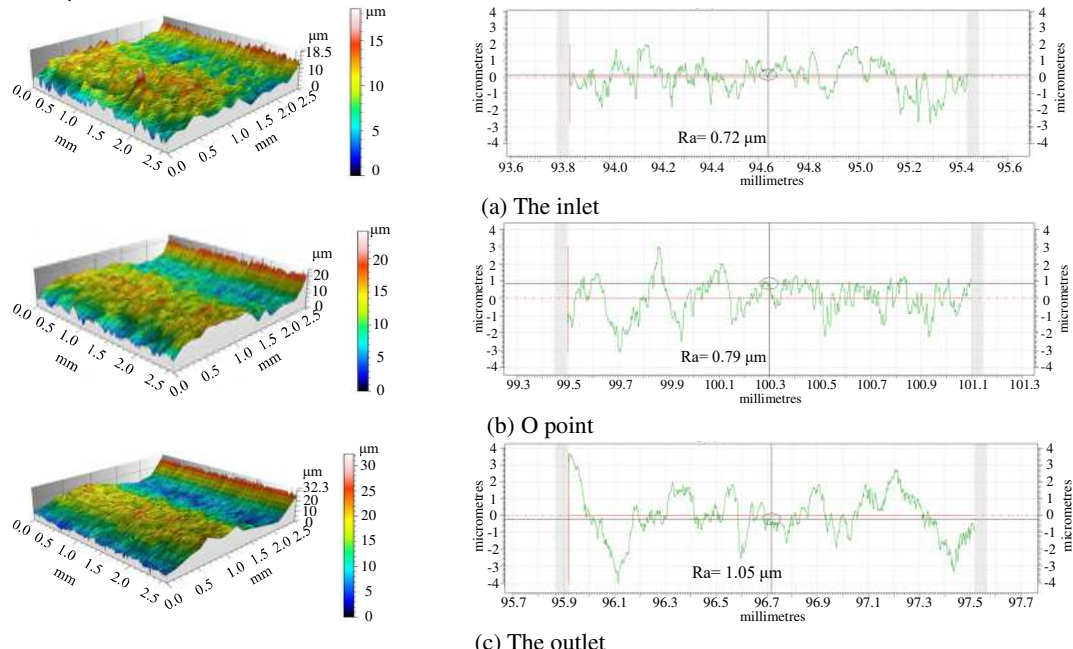


Fig.11. Three-dimensional surface topography and the surface line roughness on the line C along the flow path.

With the electrolyte flowing, the gas bubbles, the heat quantity and other processed by-products were gathered

along the flow path, resulting in the current density to gradually decrease from the inlet to the outlet. Generally, a higher current density may make the surface of the machined smoother. So, in combination with the above-mentioned influencing factors, the surface quality of the machined blade gradually deteriorated along the flow path. Therefore, the result presented was that the change of surface roughness from the inlet to the outlet was from Ra 0.72 to Ra 1.05 μm . The stray corrosion was one of the important influencing factors of surface quality. From the bottom region to the tip region along line D, the stray corrosion suffered became more serious, causing poorer surface quality.

Combined with the experiment results above, the varieties of the machining accuracy and the surface quality in each area were consistent with the simulation results. So the correctness and the effectiveness of the multiphysics coupling simulation of the ECTr were verified.

5. Conclusion

(1) A multiphysics coupling field model of ECTr was established, which involved electric field, two-phase flow field and thermal field. In this model, a coupling relationship was formed between the various physical fields through the change of the electrolyte conductivity, so that the various physical fields influenced each other. In electric field, the conductivity was an important influence factor of the current density. In flow field and temperature field, the degrees of the hydrogen evolution reaction and the current heating effect were affected by the current density. And the generated hydrogen bubbles and Joule heat affected the electrical conductivity, thereby affecting the current density. Through the multiphysics coupling field model, the physical field distribution state of ECTr that was closer to the actual processing was reflected.

(2) A multiphysics coupling field simulation in ECTr with lateral flow was carried out. Through the multiphysics coupling simulation, the distributions and varieties of the gas bubbles volume fraction, the electrolyte temperature, the electrolyte conductivity and the current density were obtained along the flow path. Compared with the inlet of the electrolyte, the gas bubbles volume fraction increased by 38.8% and the temperature increased by 6.3 K at the outlet of the electrolyte. Under the combined influence, the conductivity decreased by 7.227 S/m and the current density decreased by 57.81 A/cm² at the outlet.

(3) The experiment of lateral flow ECTr was performed. Through measuring the machined blade, the varieties of the thickness and the surface quality along the flow path were acquired. The thickness gradually increased and changed from 2.09 mm to 2.76 mm from the inlet to the outlet. Along the flow path, the surface quality gradually deteriorated and the surface roughness changed from 0.72 μm to 1.05 μm . The results between the simulations and the experiment were consistent. The multiphysics coupling simulation results were effectively verified.

Although the lateral flow can obtain a better flow state, there are certain changes in machining accuracy and surface quality along the flow path. Thus, to improve the consistency of machining quality along the flow path in lateral flow electrochemical trepanning, the pulsed machining style will be tried in future research.

Acknowledgments

This work was supported by the Joint Funds of the National Natural Science Foundation of China and Guangdong Province China [grant number U1601201], the National Natural Science Foundation of China for Creative Research Groups [grant number 51921003], and the National Science and Technology Major Project [grant number 2017-VII-0004-0097].

Declarations

Conflict of interest: The authors declare that they have no known competing financial interests or personal relationships that could have appeared to influence the work reported in this paper.

Ethical approval: This paper is new. Neither the entire paper nor any part of its content has been published or has been accepted elsewhere. It is not being submitted to any other journal as well.

Consent to participate: Not applicable.

Consent to publish: Not applicable.

References

- [1]. Klocke F, Klink A, Veselovac D, Aspinwall DK, Soo SL, Schmidt M, Schilp J, Levy G, Kruth JP (2014) Turbomachinery component manufacture by application of electrochemical, electro-physical and photonic processes. *CIRP Ann Manuf Technol* 63(2): 703-726
- [2]. Bogoveev NA, Firsov AG, Filatov EI, Tikhonov AS (2001) Computer support for “all – round” ECM processing of blades. *J Mater Process Tech* 109: 324-326
- [3]. Tang L, Feng X, Zhai KG, Ji Y, Wang Z, Lei QB, Ren L (2019) Gap flow field simulation and experiment of electrochemical machining special-shaped inner spiral tube. *Int J Adv Manuf Technol* 100: 2485-2493
- [4]. Yang F, Zhang J, Zhao S, Guo CA (2020) Analysis of flow field for electrochemical machining deep spiral hole with gradually changing groove section. *Int J Adv Manuf Technol* 107: 3267-3275
- [5]. Skinn B, Hall T, Snyder S, Rajurkar KP, Taylor EJ (2017) Accelerated electrochemical machining tool design via multiphysics modeling. *ECS Transactions* 77: 936-979
- [6]. Wang DY, Zhu ZW, Zhu D, He B, Ge YC (2017) Reduction of stray currents in counter-rotating electrochemical machining by using a flexible auxiliary electrode mechanism. *J Mater Process Tech* 239: 66-74
- [7]. Clark WG, Mcgeough JA (1977) Temperature distribution along the gap in electrochemical machining. *J Appl Electrochem* 7: 277-286
- [8]. Deconinck D, Van Damme S, Deconinck J (2012) A temperature dependent multi-ion model for time accurate numerical simulation of the electrochemical machining process. Part I: Theoretical basis. *Electrochim Acta* 60: 321-328
- [9]. Deconinck D, Van Damme S, Deconinck J (2012) A temperature dependent multi-ion model for time accurate numerical simulation of the electrochemical machining process. Part II: Numerical simulation. *Electrochim Acta* 69: 120-127
- [10]. Mi D, Luo HP, Natsu W (2018) Investigation of influence factors of surface roughness at corner area in ECM process. *Proc CIRP* 68: 709-715
- [11]. Gomez-Gallegos A, Mill F, Mount AR, Duffield S, Sherlock A (2018) 3D multiphysics model for the simulation of electrochemical machining of stainless steel (SS316). *Int J Adv Manuf Technol* 95: 2959-2972
- [12]. Klocke F, Zeis M, Klink A (2015) Interdisciplinary modelling of the electrochemical machining process for engine blades. *CIRP Ann Manuf Technol* 64: 217-220
- [13]. Chang CS, Hourng LW (2001) Two-dimensional two-phase numerical model for tool design in electrochemical machining. *J Appl Electrochem* 31: 145-154
- [14]. Schaarschmidt I, Zinecker M, Hackert-Oschätzchen M, Meichsner G (2017) Multiscale multiphysics simulation of a pulsed electrochemical machining process with oscillating cathode for microstructuring of impact extrusion punches. *Proc CIRP* 58: 257-262
- [15]. Zhu D, Gu ZZ, Xue TY, Liu A (2017) Simulation and experiment investigation on a dynamic lateral flow mode in trepanning electrochemical machining. *Chin J Aeronaut* 30(4): 1624-1630
- [16]. Gu ZZ, Zhu WG, Zheng XH, Bai XM (2019) Cathode tool design and experimental study on electrochemical trepanning of blades. *Int J Adv Manuf Technol* 100: 857-863
- [17]. Klocke F, Zeis M, Harst S, Klink A, Veselovac D, Baumgartner M (2013) Modeling and simulation of the electrochemical machining (ECM) material removal process for the manufacture of aero engine components. *Proc CIRP* 8: 265-270
- [18]. Zhou XC, Cao CY, Wang HX, Lin H (2020) Study on the multi-field coupling model of electrolyte temperature distribution in electrochemical machining. *Int J Adv Manuf Technol* 109: 1655-1662
- [19]. Chen YL, Liu Z, Zhang JC, Wang YD (2018) Multi-physics coupling simulation of precise electrochemical machining (PECM) with pulsed current and vibrating cathode. *Mat Sci Eng* 392: 032020
- [20]. Zhu D, Gu ZZ, Xue TY, Zhu D (2016) Flow field design in electrochemical machining of diffuser. *Proc CIRP* 42: 121-124
- [21]. Rajurkar KP, Zhu D, Mcgeough JA, Kozak J, Silva AD (1999) New developments in electro-chemical machining. *CIRP Ann Manuf Technol* 48 (2): 567–579
- [22]. Wang H, Zhu D, Liu J (2019) Improving the accuracy of the blade leading/trailing edges by electrochemical machining with tangential feeding. *CIRP Ann Manuf Technol* 68: 165-168
- [23]. Tijum RV, Pajak PT (2008) Simulation of production processes using the multiphysics approach: the electrochemical machining process. *Proc Eur COMSOL Conf, Hannover*
- [24]. Hu XY, Zhu D, Li JB, Gu ZZ (2019) Flow field research on electrochemical machining with gas film insulation. *J Mater Process Tech* 267: 247-256
- [25]. Fujisawa T, Inaba K, Yamamoto M (2008) Multiphysics simulation of electrochemical machining process for three-dimensional compressor blade. *J Fluid Eng* 130(8): 081602
- [26]. Kozak J (2004) Thermal models of pulse electrochemical machining. *B Pol Acad Sci-Tech* 52 (4): 313–320

Figures

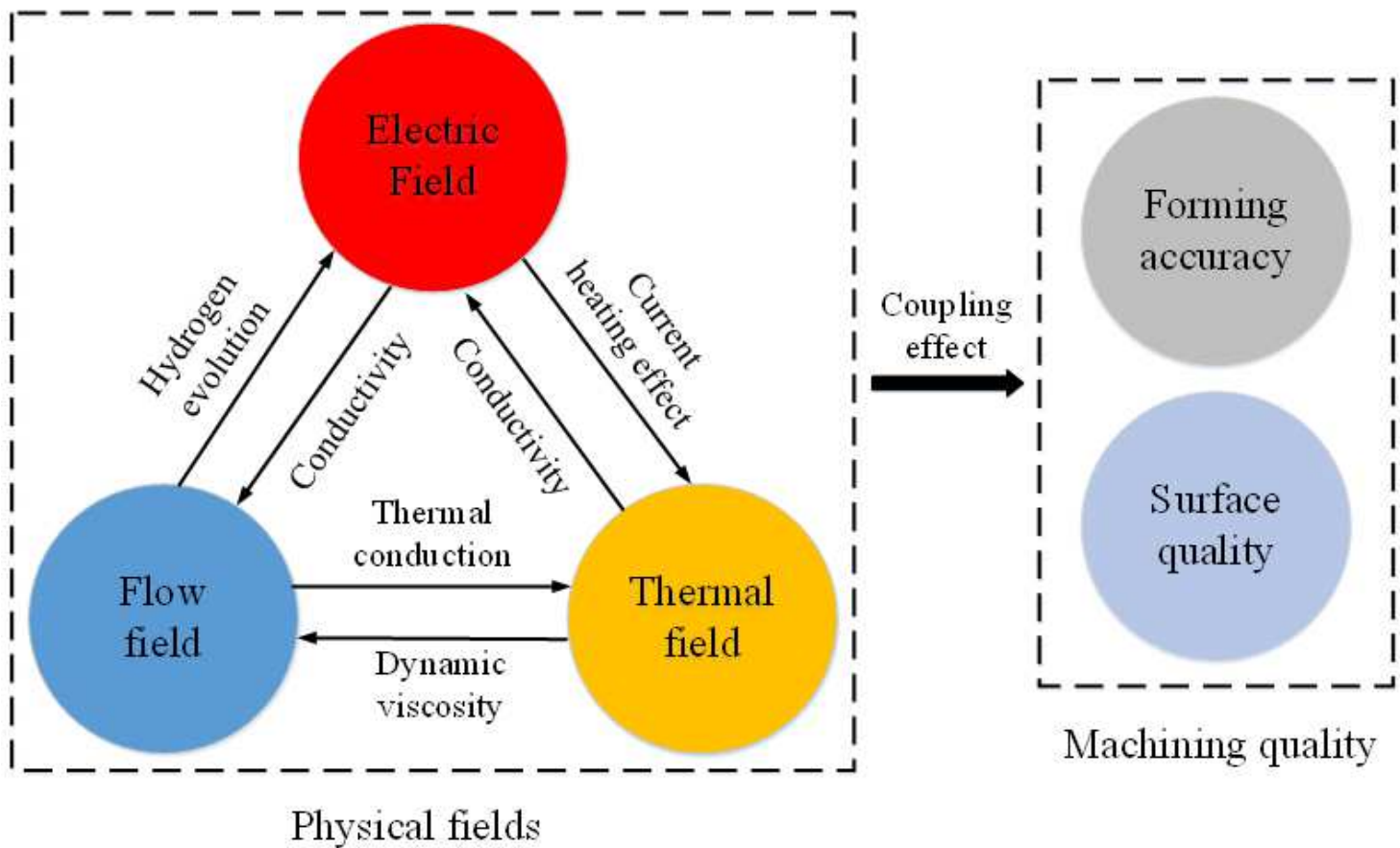


Figure 1

Relationship between physical fields and machining quality in ECM.

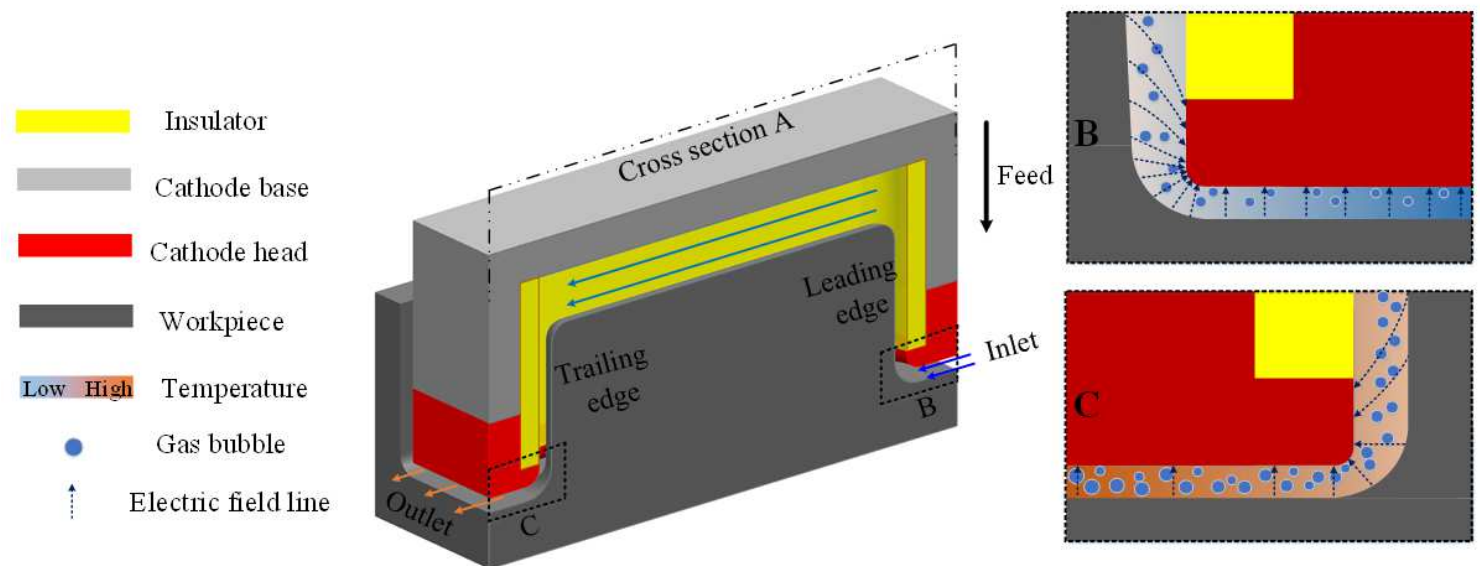


Figure 2

Schematic diagram for ECTr of lateral flow.

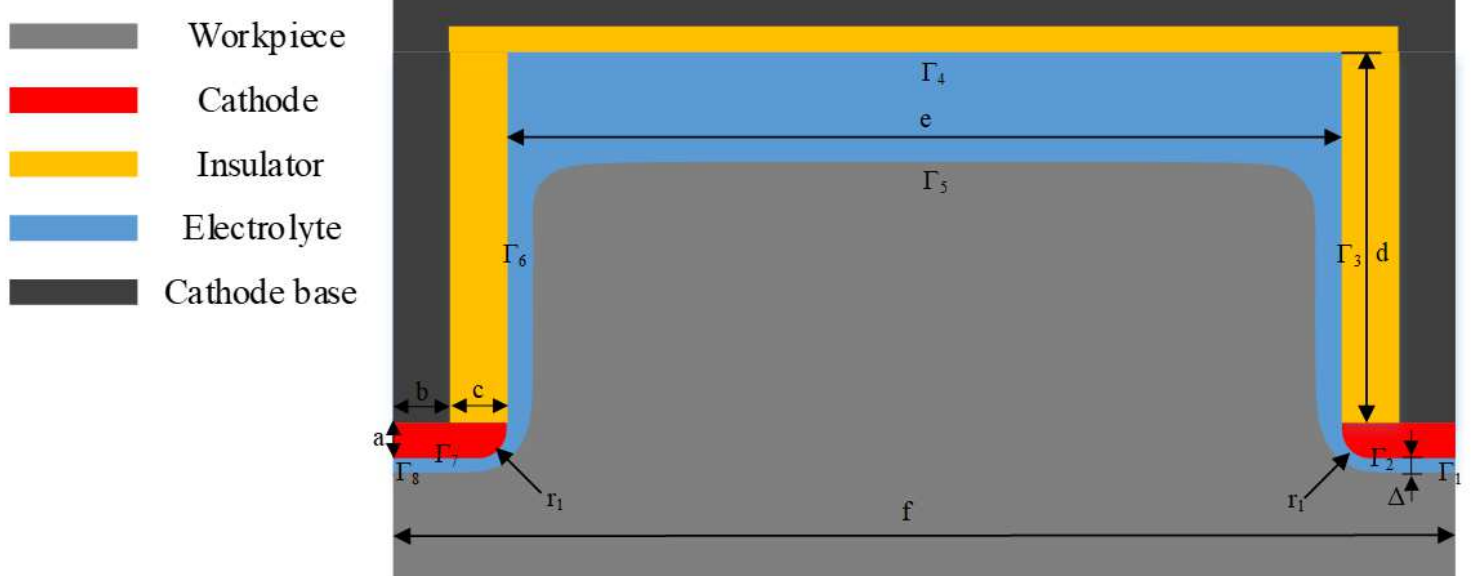


Figure 3

Simulation geometric model of ECTr with lateral flow.

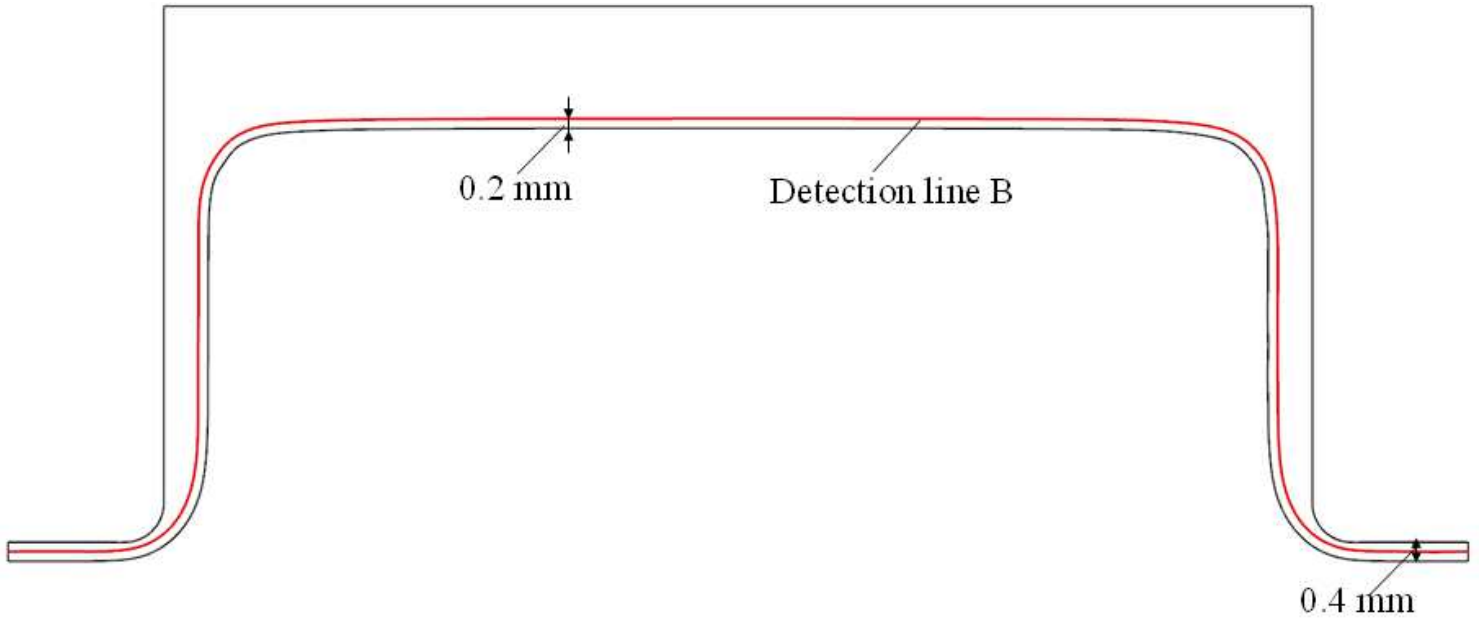
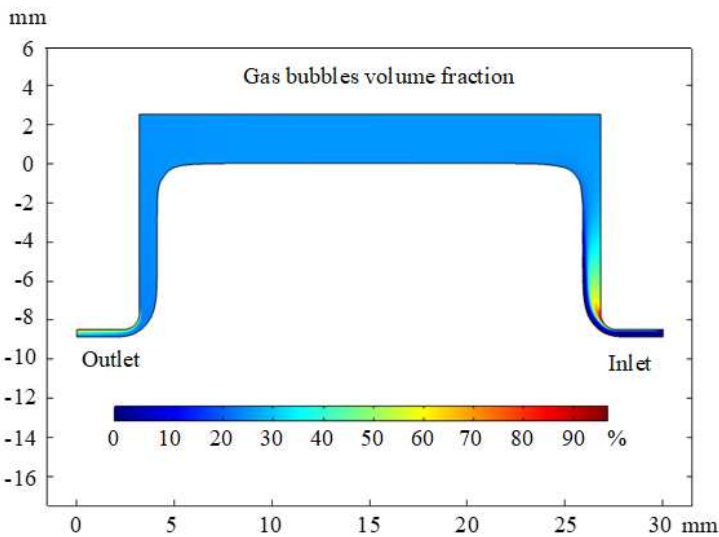
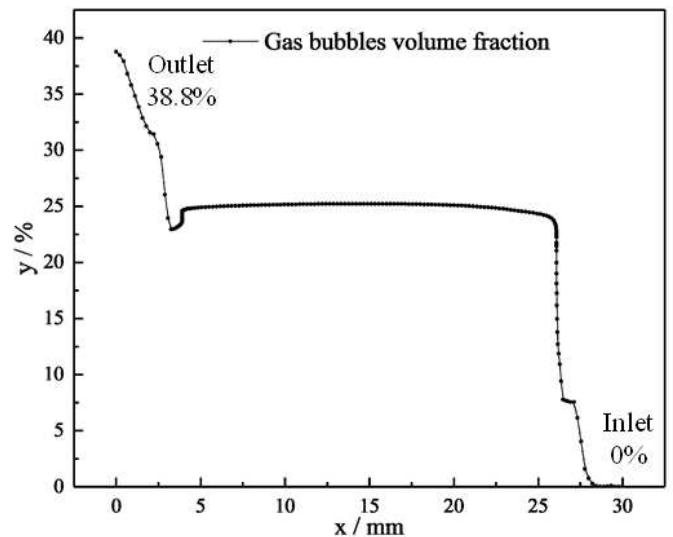


Figure 4

Detection line in the simulation.



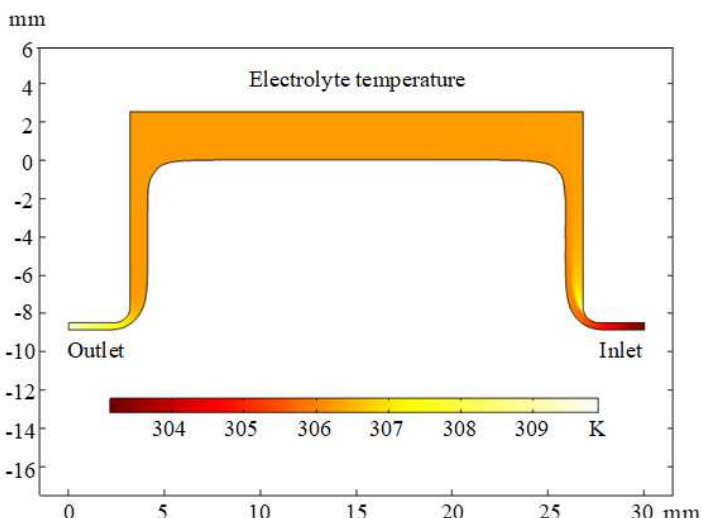
(a) Cloud



(b) Curve

Figure 5

Distribution cloud and change curve of the gas bubbles volume fraction.



(a) Cloud

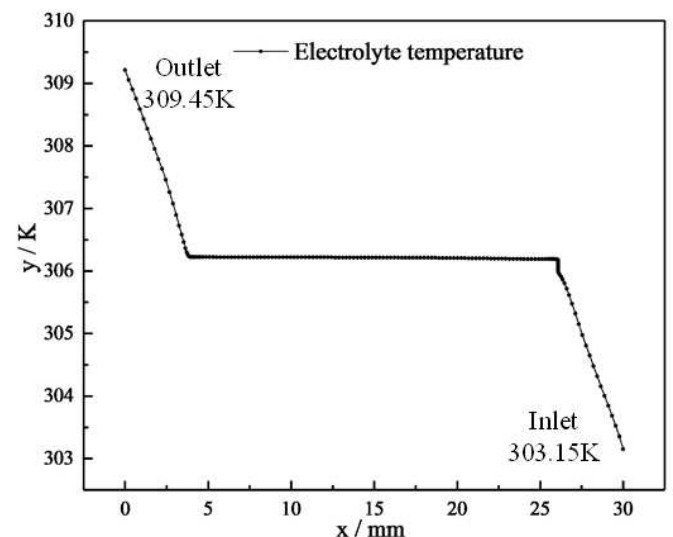
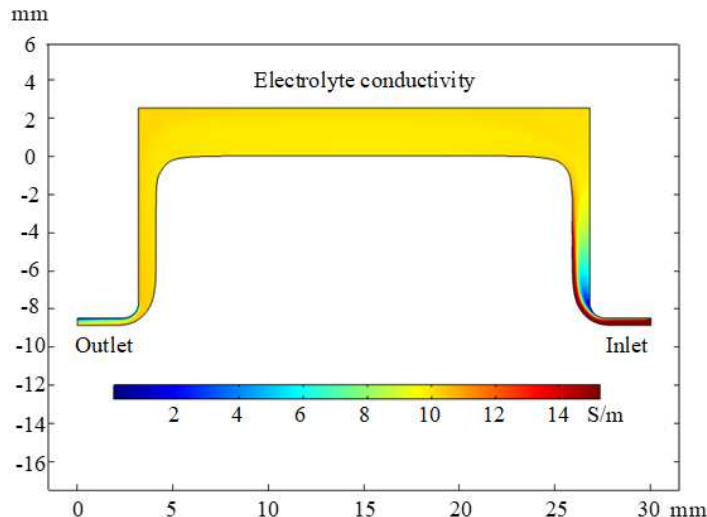
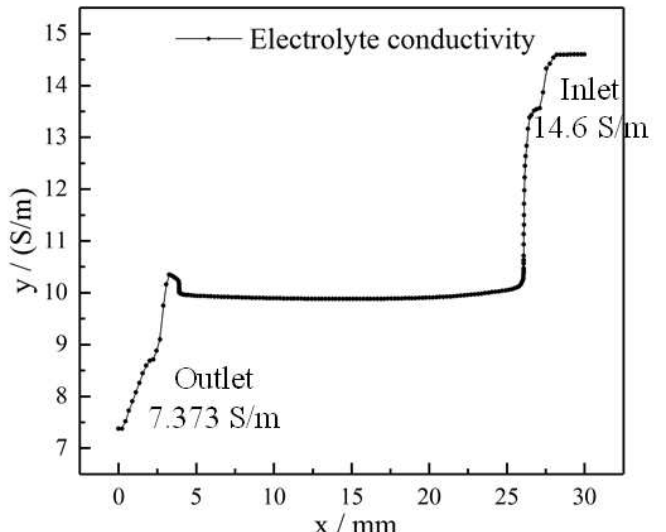


Figure 6

Distribution cloud and change curve of the electrolyte temperature.



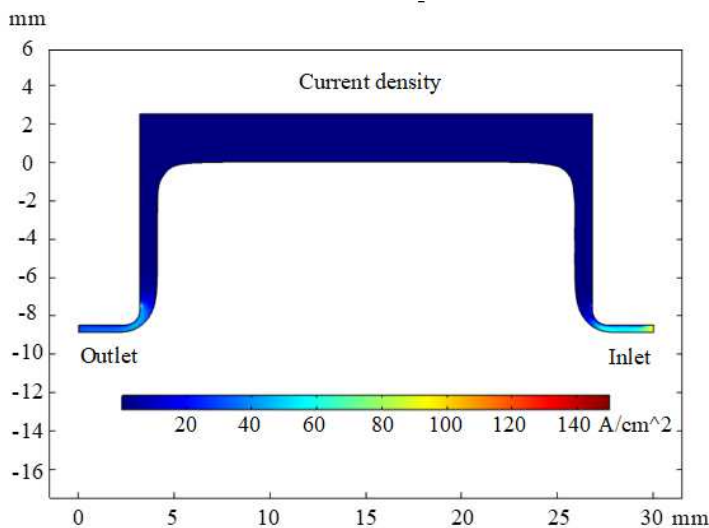
(a) Could



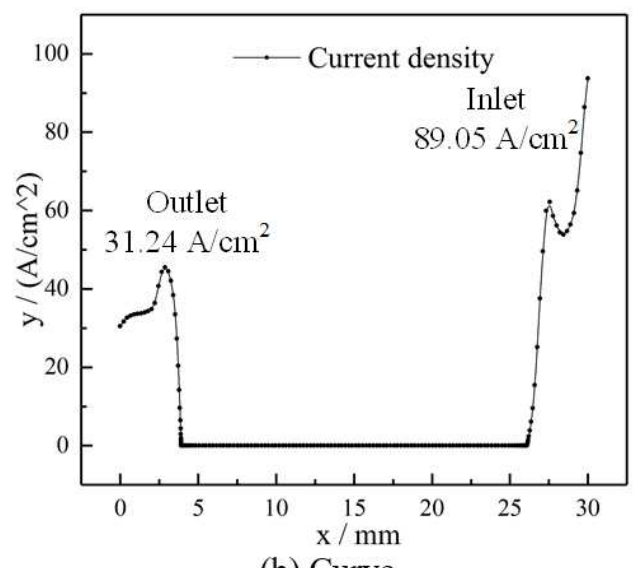
(b) Curve

Figure 7

Distribution cloud and change curve of the electrolyte conductivity.



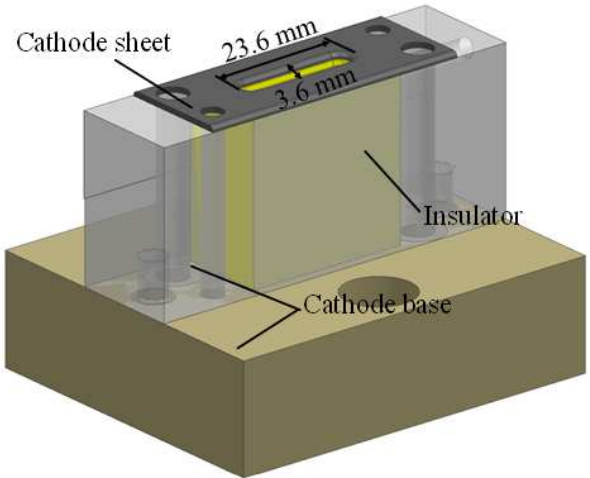
(a) Cloud



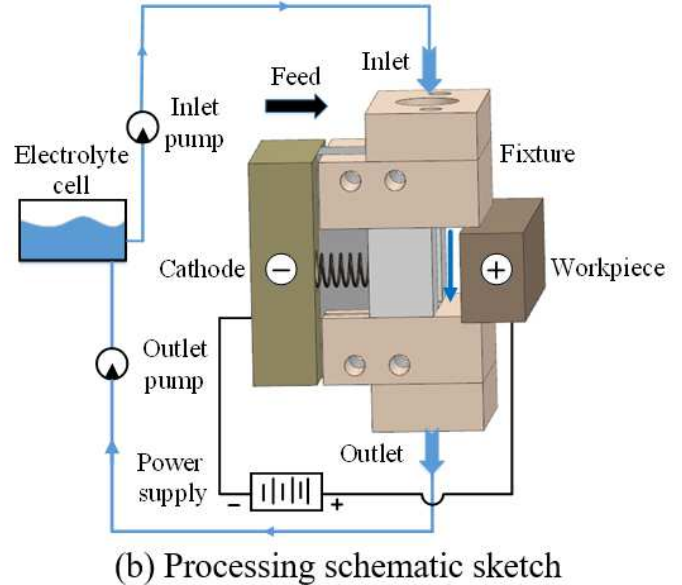
(b) Curve

Figure 8

Distribution cloud and change curve of the current density.



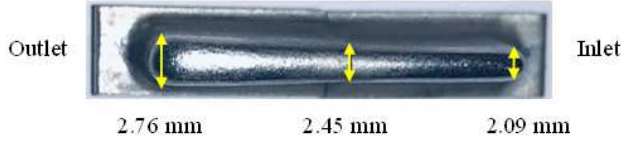
(a) Combined cathode



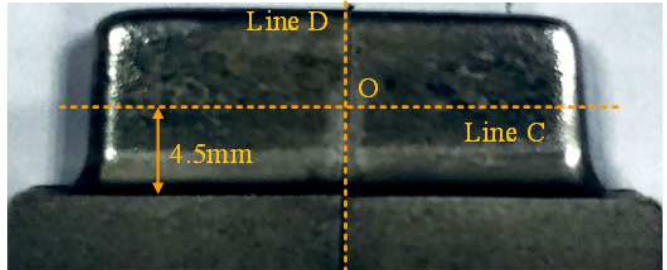
(b) Processing schematic sketch

Figure 9

Experiment set-up for lateral ECTr.



(a) Machined blade



(b) Detection lines

Figure 10

Machined blade and the detection lines on the machined blade.

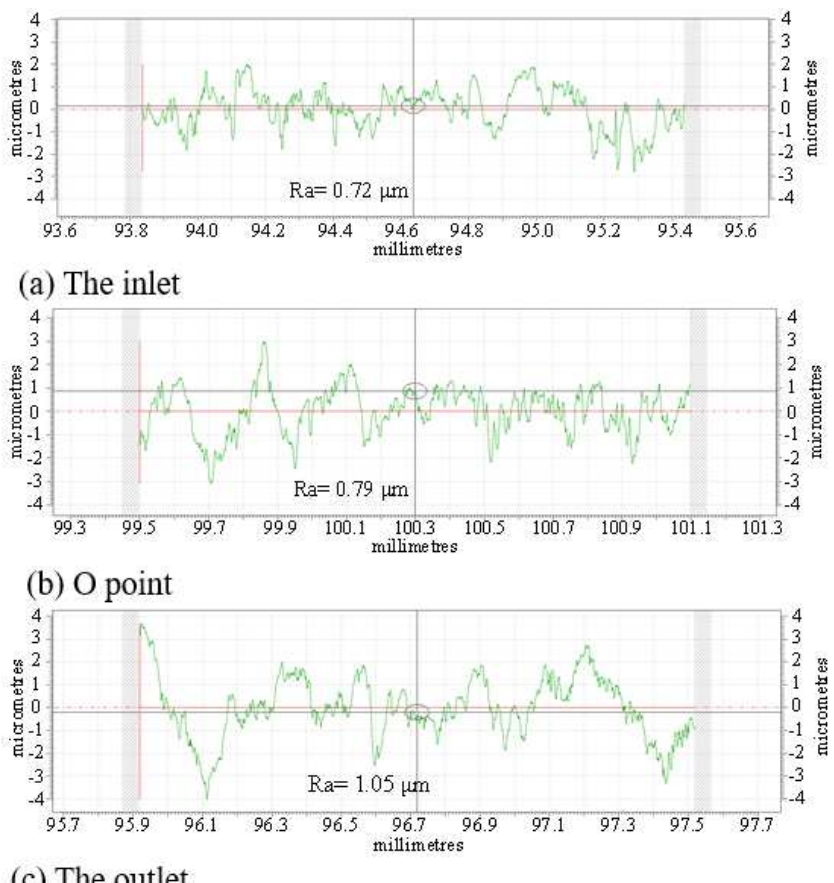
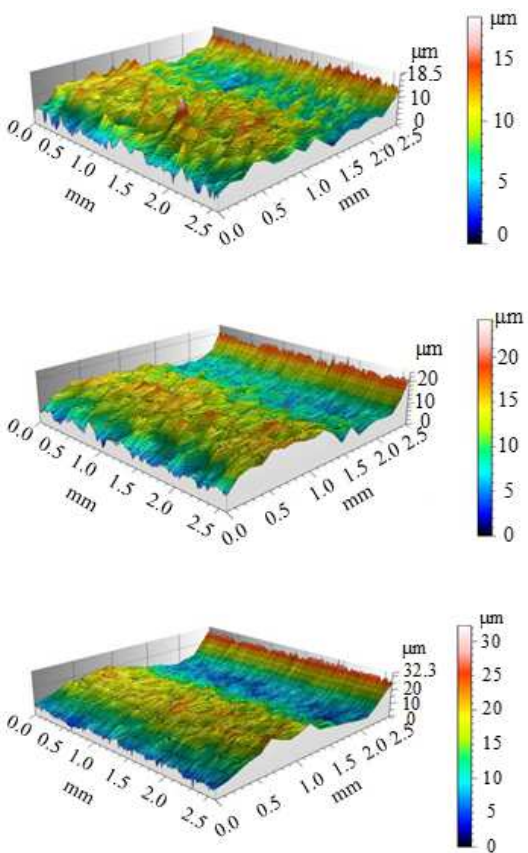


Figure 11

Three-dimensional surface topography and the surface line roughness on the line C along the flow path.